



Limits on the Density of the Lunar Ionosphere: ARTEMIS Observations

Han-Wen Shen¹ , Jasper S. Halekas¹ , and Andrew R. Poppe² ¹Department of Physics and Astronomy, University of Iowa, Iowa City, IA, USA; han-wen-shen@uiowa.edu²Space Sciences Laboratory, University of California at Berkeley, Berkeley, CA, USA

Received 2023 August 14; revised 2023 October 17; accepted 2023 October 18; published 2023 November 22

Abstract

The Moon of our Earth has a tenuous atmosphere, known as an exosphere. The ionization of this exosphere is speculated to possibly form a weak ionosphere. Some radio occultation (RO) experiments have suggested the presence of a dense ionosphere with an electron density on the order of hundreds of cm^{-3} near the surface. Using in situ measurements from the ARTEMIS mission during 2012–2021, we conduct statistical analyses and case studies to investigate the plasma density at near-surface altitudes. ARTEMIS measurements reveal no plasma densities at altitudes between 10 and 50 km that exceed 35 cm^{-3} , and therefore they provide no evidence for a steady-state or global lunar ionosphere at the level suggested by some RO observations. Density profiles with local time and altitude show higher density in the sunlit sector than in the shadowed sector. These observations suggest that the natural variation of solar wind plasma flux with solar zenith angle plays a critical role in controlling the plasma population near the surface. This research provides a reference for a comparison with RO observations and a statistical view of the low-altitude plasma environment near the lunar surface.

Unified Astronomy Thesaurus concepts: [The Moon \(1692\)](#); [Lunar science \(972\)](#); [Solar wind \(1534\)](#); [Space plasmas \(1544\)](#)

1. Introduction

The Moon, the natural satellite of the Earth, has a tenuous surface-bound exosphere without the protection of a global intrinsic magnetosphere (Stern 1999). This tenuous exosphere consists of neutral particles produced from different processes, such as solar wind implantation and outgassing, micrometeoroid impact, radiogenic decay in the lunar subsurface and subsequent outgassing, liberation of material from the regolith by charged particle and photon sputtering, and chemical and thermal release (Stern 1999; Sarantos et al. 2012; Cook et al. 2013). Some of these processes can also produce charged particles along with neutrals (e.g., Elphic et al. 1991). Meanwhile, photoionization, electron-impact ionization, and charge exchange may produce ions and electrons from the exosphere, possibly forming an ionosphere (Saranos et al. 2012; Huebner & Mukherjee 2015; Halekas et al. 2018). The in situ measurements from the Suprathermal Ion Detector Experiments (SIDE) instruments on board the Apollo missions suggested that the ion density produced by the lunar surface is lower than 10 cm^{-3} at altitudes below 100 km (Reasoner & Burke 1972; Stern 1999; Stubbs et al. 2011). The electron density of the lunar ionosphere was theoretically estimated by Bauer (1996) to be not more than 1 cm^{-3} . Such low plasma density was attributed to the motional electric field induced by the moving magnetic field of the solar wind, which sweeps away charged particles into interplanetary space, preventing an accumulation of freshly produced ions and electrons (Johnson 1971; Hodges et al. 1974).

The refractive index of an ionosphere depends on its electron density and the frequency of the electromagnetic wave passing through it (Murkett 1979), enabling radio waves to be utilized to derive the electron column concentration between a

transmitter and receiver. Results at odds with the traditional picture of the lunar ionosphere stated above were derived from several radio occultation (RO) experiments. The earliest set of lunar electron density profiles was obtained from stellar RO experiments using the Crab Nebula observations, which showed a density peak near the lunar surface with a magnitude of 1000 cm^{-3} and an exponential decrease with altitude (Elsmore 1957). This result was later supported by RO measurements on board the Luna 19 and 22 spacecraft, which inferred electron densities of $500\text{--}1000 \text{ cm}^{-3}$ above the dayside lunar surface (Vyshlov 1976; Vyshlov & Savich 1979). Recently, RO measurements were widely performed by several spacecraft missions around the Moon. Dual-frequency observations in the S band and X band by SMART-1 suggested a lunar ionosphere with a density of $\sim 100 \text{ cm}^{-3}$ (Pluchino et al. 2008). A subset of 16 single-spacecraft RO observations (4% of total observations) from the Kaguya mission statistically showed a peak density of 300 cm^{-3} with a scale height of 7 km occurring at altitudes around 30 km at solar zenith angles smaller than 60° (Imamura et al. 2012). With a two-way RO technique, the polar-orbiting Chandrayaan-1 mission inferred a peak density around 300 cm^{-3} near the terminators at high latitudes (Choudhary et al. 2016). Using RO experiments conducted on the Chandrayaan-2 spacecraft, Tripathi et al. (2022) reported that the electron content near the surface is larger on the nightside than on the dayside, supporting the prediction of a three-dimensional photochemical model (Ambili & Choudhary 2022). This model predicts that the density peak can exceed $1.2 \times 10^5 \text{ cm}^{-3}$ if the lunar environment is not interacting with the solar wind. When the electromagnetic pickup of the solar wind is taken into account, the maximum density is predicted to be 1600 cm^{-3} .

In summary, many RO observations suggest that the plasma density near the lunar surface can be on the order of hundreds of cm^{-3} ; however, there are few surveys of in situ density measurements near the surface. Through the plasma density derived from plasma oscillations shown in electric field power



Original content from this work may be used under the terms of the [Creative Commons Attribution 4.0 licence](#). Any further distribution of this work must maintain attribution to the author(s) and the title of the work, journal citation and DOI.

spectra observed by the Acceleration, Reconnection, Turbulence, and Electrodynamics of Moons Interaction with the Sun (ARTEMIS) mission, Halekas et al. (2018) statistically investigated the charged particle density in the lunar environment when the Moon passes through the Earth’s magnetotail. Their results showed day–night asymmetric and dawn–dusk symmetric distributions in the charged particle density. The ARTEMIS results suggested that a tenuous lunar ionosphere with an average density of $0.1\text{--}0.3\text{ cm}^{-3}$ exists at least 50% of the time in the magnetotail. The range of this reported density is orders of magnitude lower than those derived from RO experiments and photochemical models. The lunar ionosphere is believed to be highly variable, with various factors controlling its plasma density, including the interaction with the solar wind. Using ten years of in situ measurements from the ARTEMIS mission, we statistically examine the plasma density at altitudes near the lunar surface and derive the density profiles with altitude and local time for times when the Moon is exposed to the solar wind. In addition, we investigate two events in which one of the ARTEMIS probes sampled a low altitude (below 30 km) near the surface. Our results can be utilized as a comparison with RO experimental results.

2. ARTEMIS Data

The ARTEMIS mission consists of two identical probes, which were redeployed from five probes of the Time History of Events and Macroscale Interactions during Substorms (THEMIS) mission (Angelopoulos 2008, 2011). Each of the ARTEMIS probes orbits around the Moon near the equatorial plane ($\sim 10^\circ$ inclination) along elliptical trajectories with apselenes of $\sim 19,000$ km and periselenes with variable altitudes from about 10 to 1000 km, enabling us to investigate the plasma density near the lunar surface. The two ARTEMIS probes carry identical science instruments. The data used in the present study were obtained by the electrostatic analyzer (ESA; McFadden et al. 2008a, 2008b), electric field instruments (EFI; Bonnell et al. 2008), and fluxgate magnetometer (FGM; Auster et al. 2008) on each probe.

The FGM measures the in situ magnetic field and its low-frequency (up to 64 Hz) fluctuations, and can detect variations of the magnetic field with amplitudes as low as 0.01 nT. The EFI is designed to measure electric fields in three directions, and it provides onboard-computed electric field power spectra, covering the frequency range from DC to 8 kHz. A proxy for the spacecraft-to-plasma potential (hereinafter referred to as spacecraft potential), obtained by measuring the potential of Langmuir sensors relative to the spacecraft, is also provided by the EFI. It is known that the spacecraft potential depends on the surrounding electron density and temperature. A computer code converting the spacecraft potential to the electron density was developed by Nishimura et al. (2013) using a theoretical method proposed by Mozer (1973) and Pedersen et al. (1998). We include the electron density (Ne_{scpot}) derived from the spacecraft potential through this code in our examinations.

The ESA consists of two sensors (for ions and electrons) that sweep out 4π steradians per ~ 4 s spin period, with $180^\circ \times 6^\circ$ instantaneous fields of view, to measure ions over an energy range of 1.6 eV–25 keV and electrons over an energy range of 2 eV–32 keV. These energy ranges generally cover most of the ambient plasma. The ion and electron omnidirectional particle distributions measured by the ESA are formatted into several types of data products. “Full packets” include particle

distributions that have 32 energy and 88 solid-angle sampled bins with a low cadence of 32 spins per distribution in the fast-survey mode or 128 spins per distribution in the slow-survey mode (we note that the probe spin period is ~ 4 s). In contrast, the particle distributions collected in “Reduced packets” are sampled with a high cadence of one spin per distribution, but with lower angular and energy resolutions. “Burst packets” contain particle distributions binned by the full 32 energies and 88 solid angles with spin-period time resolution, but are only available for a few short intervals (about 5 minutes per day), due to telemetry limitations.

Based on three-dimensional particle distributions measured by the ESA, plasma moments are computed on board with one-spin resolution. These moments include the ion and electron densities, three-component number fluxes, six-component momentum tensors, and three-component energy fluxes. The moment computations include a correction for the measured spacecraft potential and therefore take into account spacecraft charging effects. The spacecraft potential is used to correctly shift the energies of particles in the moment computations. This correction can effectively eliminate spacecraft-generated (i.e., nongeophysical) photoelectrons that often contaminate electron measurements and could otherwise result in large errors in the electron density calculation. The correction with the spacecraft potential allows the electron density moment computations to include only electron counts within energy bins above the potential. However, there could still be minor errors in this correction. The extremely cold (with energies of only a few eV) ambient electrons (if they exist) within the same discrete energy bin as the spacecraft potential could be thrown away from the moment computations. In this case, the electron density moments may be slightly underestimated, but these slight underestimations should not cause an error in verifying the presence of a dense ionosphere (i.e., with a density of hundreds cm^{-3}). The moment computations also include a correction with weighting factors for energy and angle efficiency variations in the sensors (McFadden et al. 2008a, 2008b).

The spacecraft potential is critical in determining whether the entire cold electron population can be measured. As illustrated by Figure 1, all ambient electrons will be accelerated when the spacecraft potential is positive (which is almost always the case when sunlit, due to photoemission). If the potential has a large enough positive value, all the cold electrons that would otherwise be excluded from the measurement range will gain sufficient energy to be measured after acceleration. In contrast, a portion of the cold ions (if any are present) may be excluded from the measurement range for positive spacecraft potentials. In sunlight, the ARTEMIS probes typically have a sufficiently large positive potential to enable measurement of the entire cold electron population. In shadow, the spacecraft potential generally lies near zero, thanks to active biasing of the EFI (Halekas et al. 2011). Therefore, in shadow, some fraction of both cold electrons and cold ions (if present) could be missed.

Data-quality flags for density moments measured by the ESA are attached in high-level processed data (Level 2), which provide a reference for identifying possible issues in the data. A flag value of “0” indicates that the corresponding data currently have no issues and are good for scientific investigations. A nonzero flag value indicates that there may be problems with the corresponding data. For example, the value “1” means that there is no spacecraft potential available, and thus photoelectrons are included in moment computations and could lead to

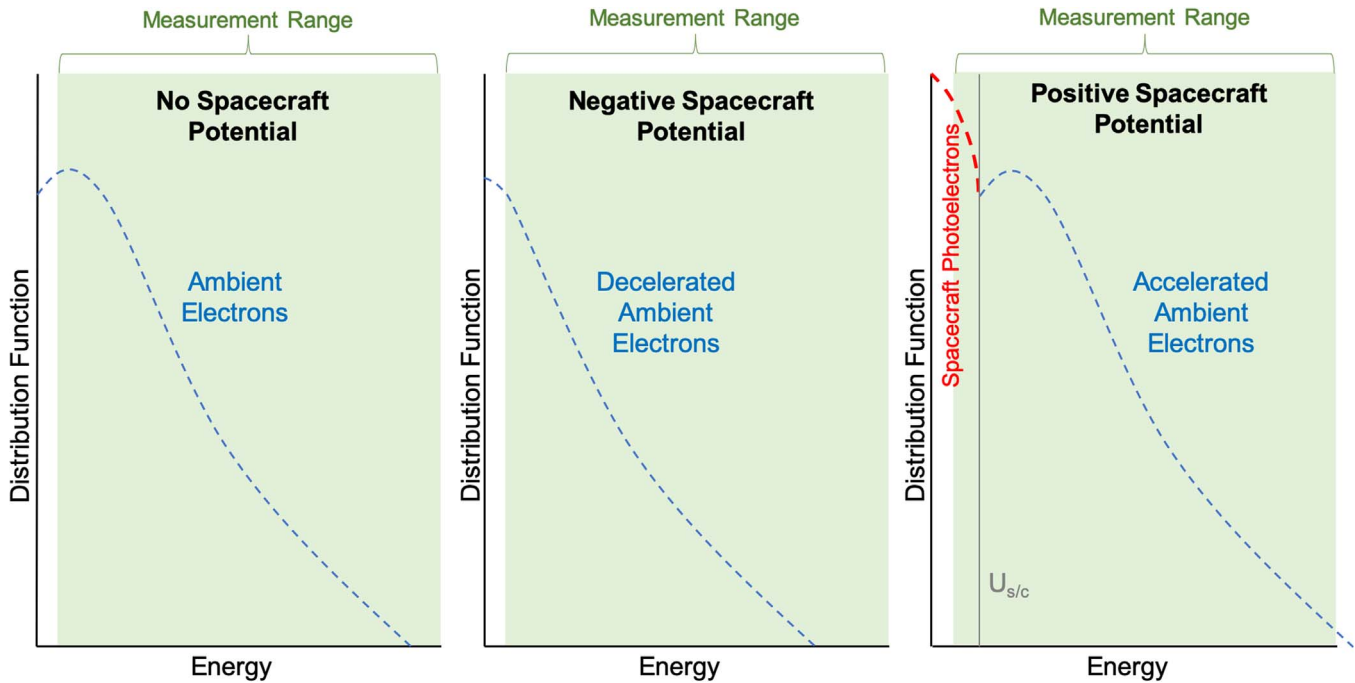


Figure 1. Schematic illustration showing the effects of spacecraft potential on measurements of the electron energy spectrum. Measured electron spectra are illustrated for three different conditions of spacecraft potential. In each spectrum, the blue dashed curve indicates the energy distribution function of the ambient electrons (which is the same in all three cases, but shifted in energy due to the spacecraft potential). In the spectrum for positive spacecraft potential, the red curve indicates the energy distribution function of spacecraft-generated (i.e., nongeophysical) photoelectrons, and the gray vertical line indicates the spacecraft potential ($U_{s/c}$).

overestimated values for electron moments. More detailed descriptions of nonzero flag values can be found in McFadden et al. (2008a). We use only the density moment data flagged with “0” for our later analyses. Three types of density data are compared in the present study, including the ion and electron density moments (Ni_mom and Ne_mom) measured by the ESA, as well as the electron density (Ne_spot) derived from the spacecraft potential.

3. Event Studies

In this section, we present two separate events when one ARTEMIS probe reached an altitude less than 30 km, with one event on the dayside and the other event on the nightside.

3.1. Dayside Event on 2013 May 10

On 2013 May 10, the ARTEMIS P2 probe reached an altitude of 18.4 km near the subsolar point, as shown in Figures 2(f) and (g). The Moon was in the undisturbed solar wind upstream of the Earth’s bow shock at this time. This event gives us a good opportunity to examine the plasma density at a low altitude near the dayside lunar surface. The qualities of density moment data for the whole interval of this event are indicated as being good, with quality flags of “0”. From Figure 2(c), we find no significant variations in the three density measurements (Ni_mom , Ne_mom , and Ne_spot), which all remain at a magnitude lower than 5 cm^{-3} during this interval, indicating no measured densities as high as the level observed by RO experiments at this near-surface altitude near the subsolar point. The spacecraft potential allows us to determine if the electron measurements contain cold electrons. As shown by the black line in Figure 2(b), the spacecraft potential in this interval has a steady value of 13 V, large enough to enable any cold electrons present to be measured by

the ESA instrument. Therefore, the electron density measurements shown in Figure 2(c) should not be underestimated, even in the presence of any significant cold electron population. In Figure 2(b), all the electrons with energies below the spacecraft potential (denoted as the black line) are photoelectrons, which have been excluded from the electron density moment computations.

We note the presence of perturbations in the ion and electron omnidirectional energy flux spectra, magnetic field, and ion bulk velocity near the time when the probe reached the lowest altitude. These are likely related to the interaction between the incoming solar wind plasma and particles reflected from the surface and/or crustal magnetic fields. For example, the magnetic field becomes more disturbed and the ion velocity decreases near the surface, as depicted in Figures 2(d) and (e). An enhancement in the ion energy flux with energies lower than 1 keV is shown in Figure 2(a), which can be attributed to solar wind ions reflected from the surface regolith and/or small-scale remanent crustal magnetic fields (Saito et al. 2010; Lue et al. 2011; Saito et al. 2012). Figure 2(b) shows a slight energization of the low-energy electrons, which is likely related to heating by plasma instabilities associated with the reflection of charged particles by crustal magnetic fields near the surface (Halekas et al. 2008; Chu et al. 2021; Sawyer & Halekas 2022). One may argue that this slight electron energization is also possibly due to the electron acceleration caused by an antimoongward electric field over the magnetic anomaly region, as suggested by Saito et al. (2012). From the electron temperature and velocity moments (not shown in this paper), we see a significant enhancement in the electron temperature, but we do not see an increase in the electron bulk velocity by the amount expected from the electron energization shown in Figure 2(b). Therefore, this is a case of electron heating, not electron acceleration.

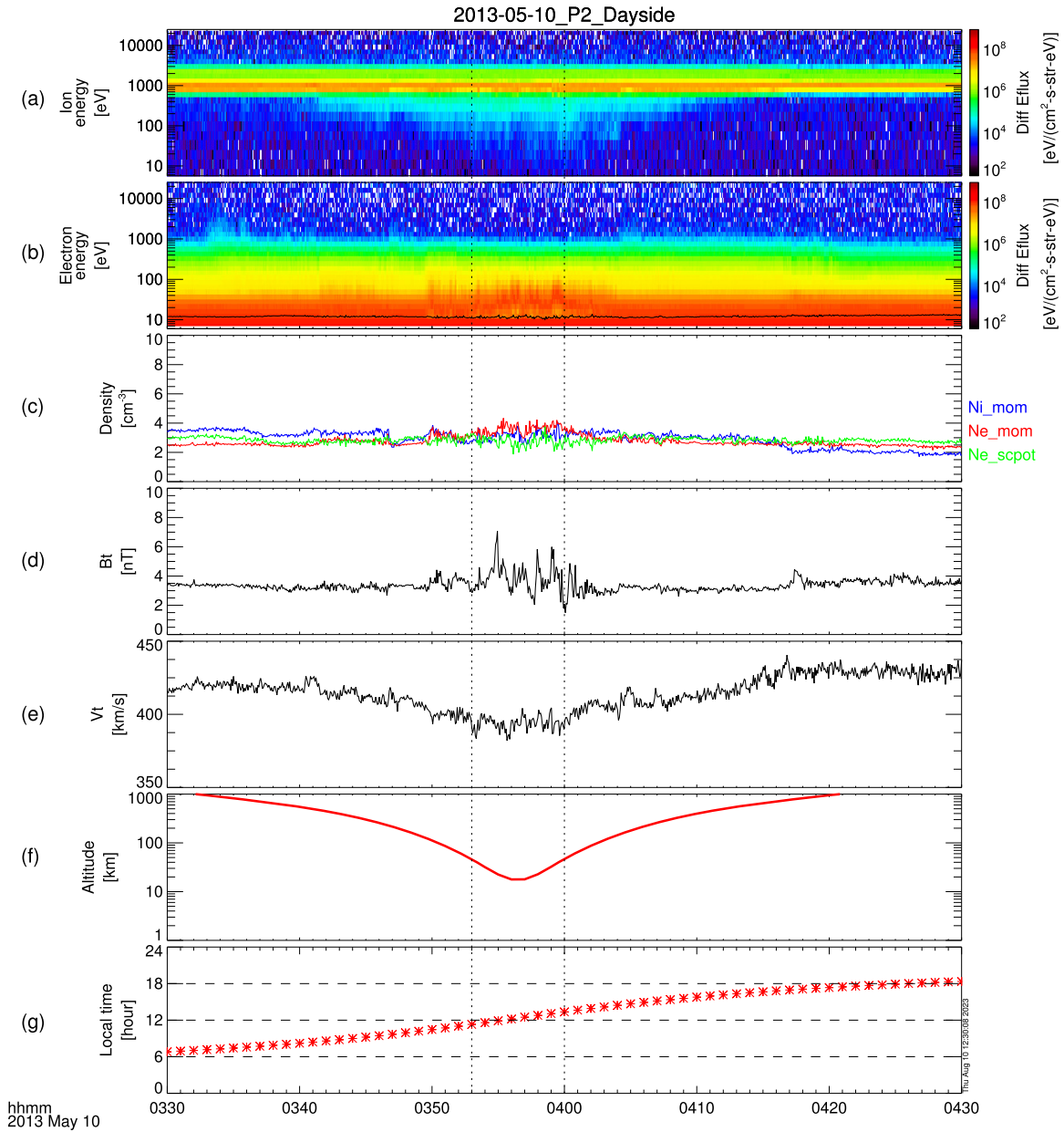


Figure 2. Measurements from the ARTEMIS P2 probe for the dayside event on 2013 May 10. The interval between the two black vertical dotted lines shows when the probe reaches altitudes below 30 km. Panels (a) and (b) show the ion and electron omnidirectional energy flux spectra, respectively. The black line in panel (b) indicates the spacecraft potential. Panel (c) displays the electron density (Ne_{scpot}) derived from the spacecraft potential and the ion and electron density moments (Ni_{mom} and Ne_{mom}) measured by the ESA. Panels (d) and (e) show variations of the magnetic field strength and ion velocity measured from the FGM and ESA, respectively. The variations in altitude and local time of the probe are presented in panels (f) and (g), respectively.

3.2. Nightside Event on 2014 February 27

Figure 3 shows variations in several plasma and magnetic field features during a period of the ARTEMIS P2 probe passing through the lunar wake on 2014 February 27. In this period, the probe reached a near-surface altitude of 20 km when it was in the lunar shadow. Because the spacecraft potential cannot be accurately measured in shadow, absent photoemission, the electron density derived from the spacecraft potential is false and thus cannot be used here for investigation. Figure 3(d) shows the ESA density moments with good-quality flags, but these flags do not include a consideration of errors caused by a biasing mode switch. Just before the probe crosses the boundary between the shadowed and sunlit region, the EFI changes its biasing mode (Halekas et al. 2011), which affects

the quality of electron density moments that utilize the spacecraft potential as an input. Both the spacecraft potential and electron density have steep drops and jumps at the beginnings and endings of these crossing intervals (marked with orange vertical dashed lines), as displayed in Figures 3(c) and (d). As a result, the electron density moments during intervals near the sunlight–shadow crossings could possess a large systematic error that alters their accuracy.

The electron density near the lunar surface in the shadowed region shown in Figure 3(d) may not be accurately measured, because of the low spacecraft potential, which may lead to incomplete coverage of cold electrons and could result in an underestimation of the electron density. However, the correctness of this measured electron density can be evaluated through

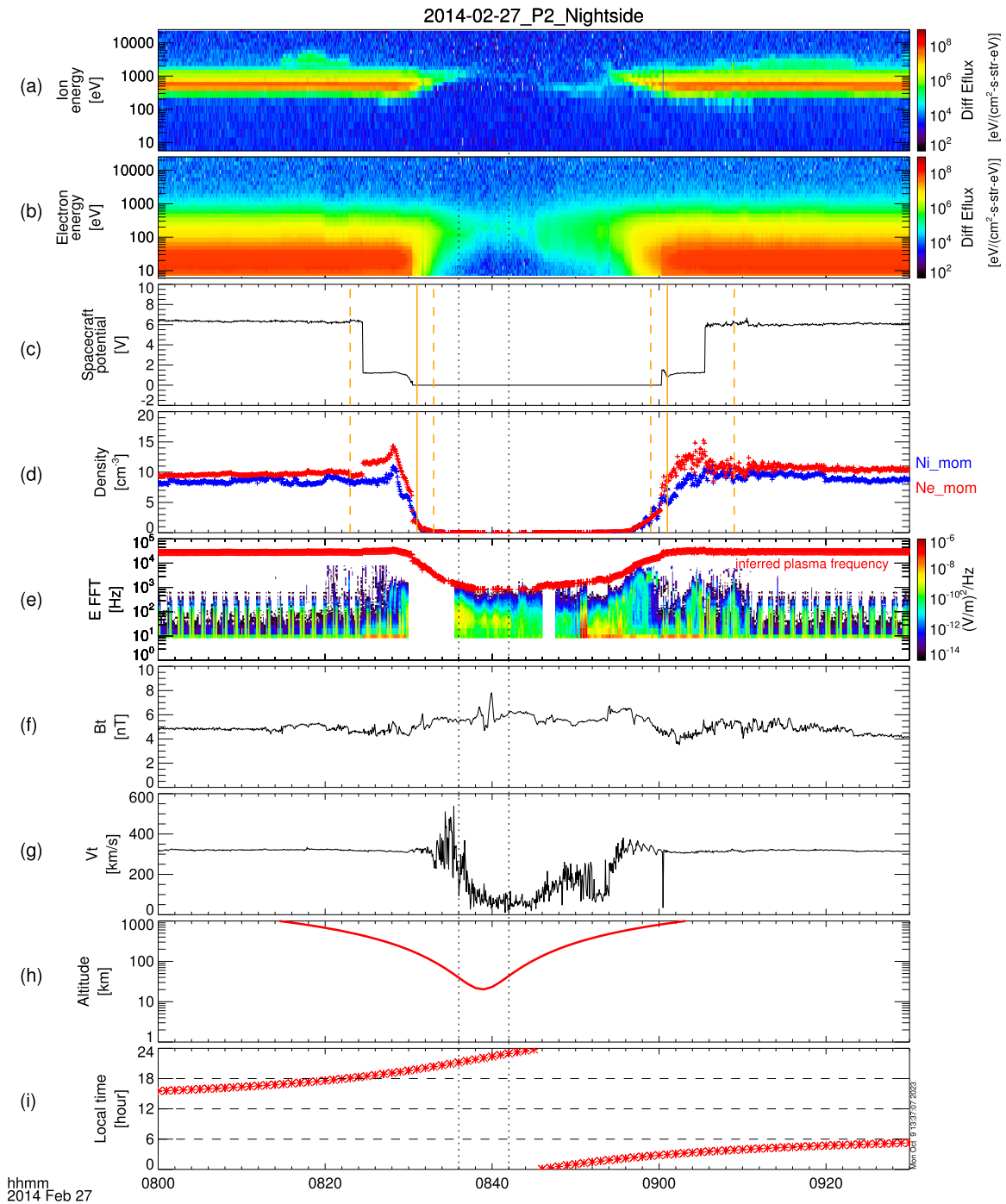


Figure 3. Measurements from the ARTEMIS P2 probe for the nightside event on 2014 February 27. The interval between the two black vertical dotted lines shows when the probe reaches altitudes below 30 km. Panels (a) and (b) present the ion and electron energy flux spectra, respectively. Panel (c) shows the spacecraft potential. Panel (d) displays the ion and electron density moments measured by the ESA. The left-hand orange vertical solid line indicates the time when the probe crossed from sunlight to shadow, and the right-hand one indicates the crossing from shadow to sunlight. The vertical dashed lines near the left-hand (right-hand) vertical solid line indicate 8 (2) minutes before and 2 (8) minutes after the time of crossing from sunlight (shadow) to shadow (sunlight). Panel (e) depicts the electric field power spectra (using Fast Fourier Transforms) observed by the EFI, and the red curve in this panel indicates the plasma frequency inferred from the measured electron density moment (Ne_mom). Panels (f)–(i) show the same variables as Figures 2(d)–(g).

plasma electrostatic oscillations shown in the electric field power spectra (Halekas et al. 2018). Physically, we can expect these electrostatic oscillations to extend up to the plasma frequency—but not above. If the measured electron densities were underestimated, we would expect to see significant signals above the plasma frequency inferred from the electron density moments. As displayed in Figure 3(e), the upper bound

of the oscillation frequency is not higher than the inferred plasma frequency, suggesting that the low electron density measured near the nightside surface can most likely be trusted. Furthermore, the electron and ion densities on the nightside match each other quite well, with both having very low values, providing additional evidence for the absence of high densities at these near-surface altitudes on the nightside. The periodic

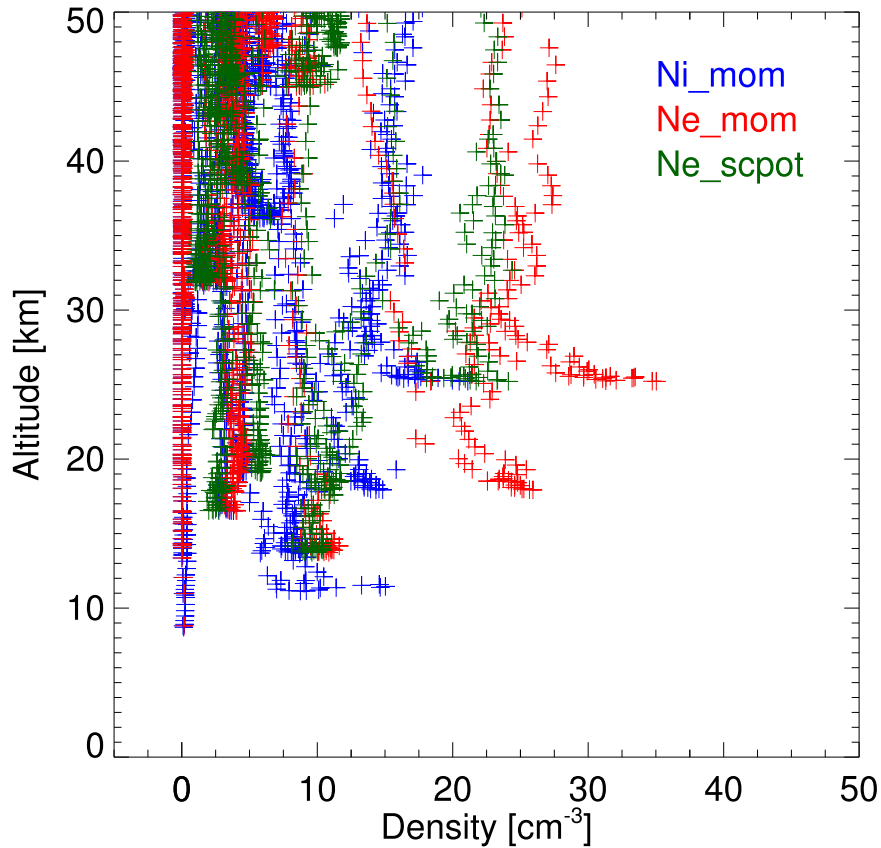


Figure 4. Scatter plot of plasma density vs. altitude near the lunar surface. The plus symbols in different colors indicate different types of all density measurements at altitudes below 50 km from the ARTEMIS mission during 2012–2021.

low-frequency EFI signals during intervals of 08:00–08:30 UT and 09:00–09:30 UT shown in Figure 3(e) are unphysical, due to the spin-shadowing of the probe in sunlight.

4. Statistical Study

We examine plasma density data measured by the ESA and derived from the spacecraft potential over a ten-year period from 2012–2021, for times when the Moon was exposed to the solar wind. For both ion and electron density moments measured by the ESA, we use only the data with good-quality flags in our statistics. For the electron density derived from the spacecraft potential (i.e., *Ne_scpot*), we only include data above the lunar dayside in our statistics, because the spacecraft potential is measured accurately only in sunlight. Because the electron density moment computations near crossings between sunlight and shadow are compromised by the EFI biasing mode switch, as described in Section 3.2, we remove the electron density samples during intervals near crossings from our data set. When either probe traveled from (to) the sunlit region to (from) the shadowed region, the compromised interval to be removed is identified as 8 minutes (2 minutes) before the crossing to 2 minutes (8 minutes) after the crossing. We remove only the electron measurements during these time periods, but not the ion measurements, which are much less affected by the mode switch. Figure 4 shows the density–altitude profile for all observations with altitudes less than 50 km and satisfying the constraints listed above. These observations were sampled from 30 orbits. In all three density data sets (i.e., *Ni_mom*, *Ne_mom*, and *Ne_scpot*), we find an average density of 5.4 cm^{-3} and no density magnitudes larger

than 35 cm^{-3} at altitudes below 50 km, as shown in Figure 4. This average value is much smaller than previous predictions by RO experiments and photochemical models in this altitude range. The lowest altitude of the ARTEMIS measurements is about 10 km, so it is possible that higher densities could exist below that altitude.

Plasma density profiles near the lunar surface in the solar wind environment as a function of altitude and local time based on in situ measurements have not previously been reported. ARTEMIS density measurements are made near the lunar equatorial plane, and therefore their corresponding solar zenith angles depend mainly on local time, with the lowest solar zenith angle near noon and the highest solar zenith angle near midnight. We can therefore examine the relation between the plasma density and solar zenith angle using density profiles as a function of local time.

Figure 5 shows the median ion and electron density profiles derived from the three types of density data as functions of altitude and local time. The lower and upper bounds of each error bar represent the first and third quartiles, respectively. The median values are computed only for the bins that contain more than ten data counts. The four panels in the left-hand column display density profiles with altitude for four local-time sectors, including nightside (22:00–02:00 local times), dawn side (06:00–08:00 local times), dayside (10:00–14:00 local times), and dusk side (16:00–18:00 local times). We choose narrower local-time ranges for the dawn and dusk profiles in order to avoid some data samples in the wake from affecting the statistics. In each of the latter three sectors stated above, the electron density is typically higher than the ion density, but

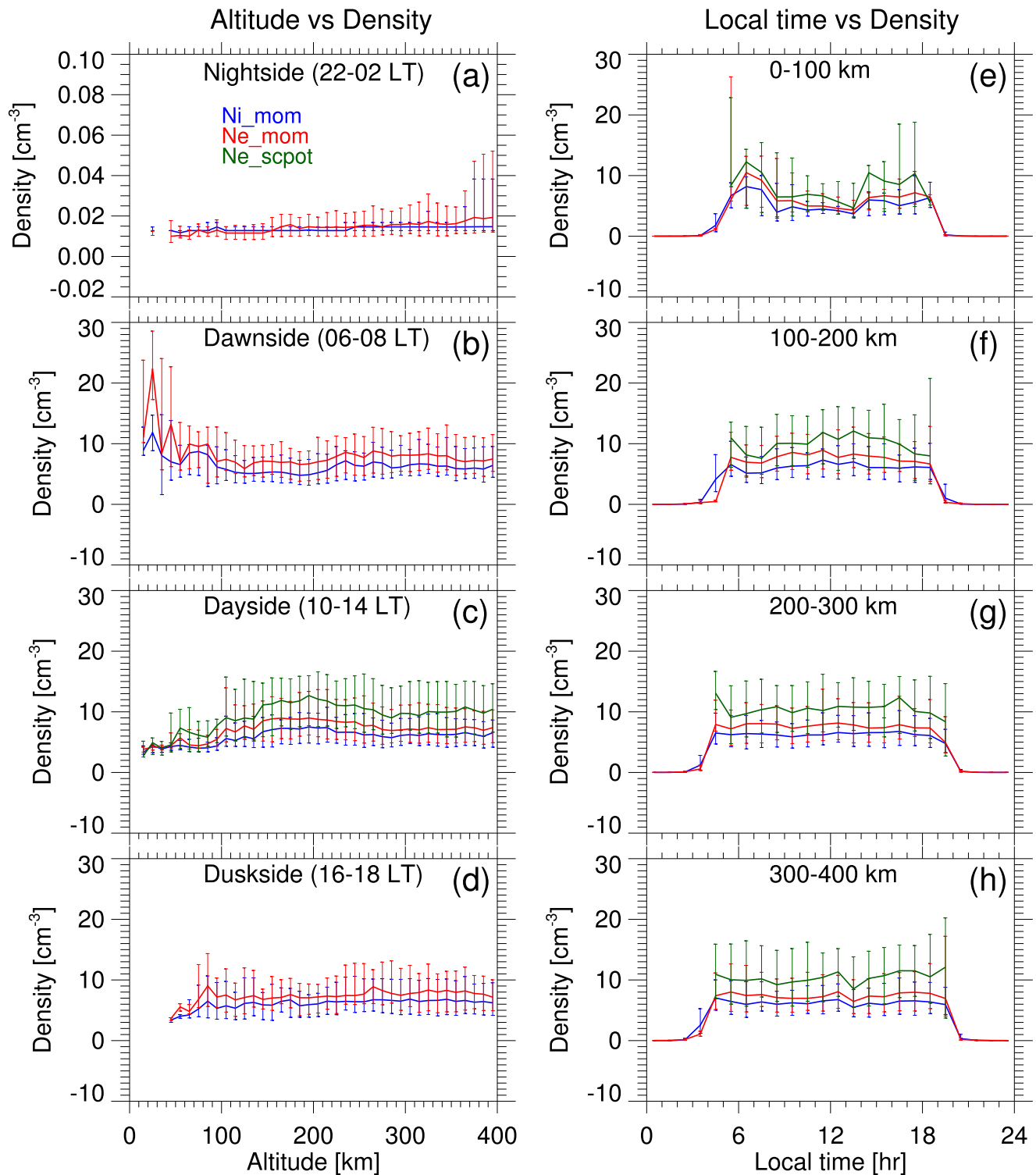


Figure 5. Plasma density profiles with altitude and lunar local time derived from ARTEMIS measurements during 2012–2021. The left-hand panels show the profiles as a function of altitude for four local-time sectors, and the right-hand panels show the profiles as a function of local time for four altitude ranges. One should note the different scale in panel (a).

with similar trends. The difference between ion and electron densities is of course unphysical, and it likely results from minor inaccuracies in the density moment computations. In sunlight, the spacecraft potential is typically large enough to ensure that all cold electrons are measured. Therefore, we expect that the measured electron densities are generally correct. The measured ion densities may be slightly

underestimated because cold ions could be excluded from the measurement range for positive spacecraft potentials, or they may be smaller than the electron densities due to saturation by the intense solar wind beam. In any case, the slight disagreement between the electron and ion density moments does not support the existence of a substantial amount of unmeasured cold ions at the density level expected by RO

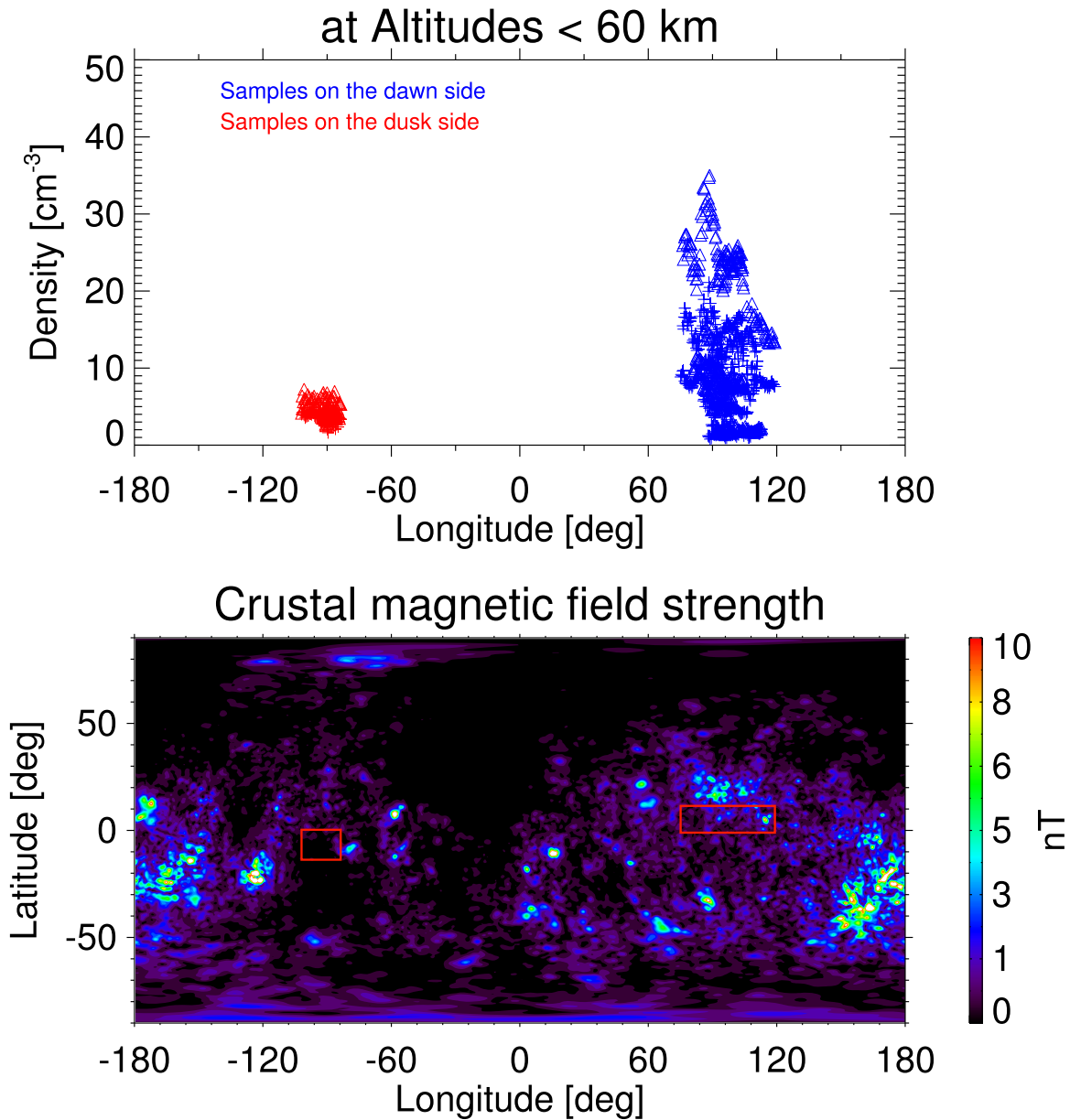


Figure 6. Dependences of plasma density on selenographic longitude and crustal magnetic field strength. The density samples are at altitudes below 60 km on the dawn (06:00–08:00) and dusk (16:00–18:00) sides. The plus and triangle symbols in the top panel indicate samples of Ni_mom and Ne_mom , respectively. The left-hand and right-hand red rectangles in the bottom panel represent the distribution ranges of samples on the dusk and dawn sides, respectively.

experiments, because we do not see a huge density difference (i.e., hundreds of cm^{-3}) between the measured ion and electron densities. The ARTEMIS observations therefore suggest that both ion and electron densities provide correct plasma density trends with altitude and local time; however, in magnitude, the actual plasma density may be closer to the measured electron density than to the measured ion density.

On the nightside, the ion and electron median densities have no significant variations with altitude, and both remain a small magnitude lower than 0.02 cm^{-3} , as shown in Figure 5(a). These low densities are characteristic of the lunar wake (Colburn et al. 1967; Ogilvie & Ness 1969; Bosqued et al. 1996; Ogilvie et al. 1996; Halekas et al. 2005). By comparing with the electric field power spectra, we have confirmed that nightside electron density measurements are most likely not underestimated. On the dawn side, the plasma density at altitudes of 60–400 km maintains a value smaller than 10 cm^{-3} ,

while there is a density enhancement at altitudes below 60 km, as shown in Figure 5(b). This density enhancement likely results from crustal magnetic field interactions with solar wind particles that produce limb compressions/shocks near the surface (Siscoe et al. 1969; Sonett & Mihalov 1972; Russell & Lichtenstein 1975; Lin et al. 1998; Halekas et al. 2014). Figure 5(c) displays density profiles with altitude on the dayside near the subsolar point. The plasma density in this local-time sector is generally between $1\text{--}10 \text{ cm}^{-3}$. Figure 5(d) shows density profiles with altitude on the dusk side, and there are no median densities higher than 10 cm^{-3} at altitudes below 400 km. The lowest altitude bin with the median densities shown in these profiles is 40–50 km. We do not see a density enhancement at altitudes below 60 km in these dusk profiles, as compared with the dawn profiles shown in Figure 5(b). We have compared selenographic longitudes of the density samples at altitudes below 60 km between these two local-time sectors.

It is found that the samples on the dawn and dusk sides are located at longitudes near 90° and -90° , respectively, as shown in the top panel of Figure 6. This difference in the longitudinal distribution between the samples on these two sides can be attributed to the orbital dynamics of the ARTEMIS spacecraft. We further project the latitudinal and longitudinal ranges of these samples onto the map of the crustal magnetic field strength (using the model of Tsunakawa et al. (2015)), as presented in the bottom panel of Figure 6. The projection shows that the samples on the dawn side are located in a region with significant crustal magnetic fields, while those on the dusk side are located in a region with very weak crustal magnetic fields. This difference in the corresponding crustal magnetic field strength is a likely cause of differences in the density at altitudes below 60 km between these two local-time sectors.

The four right-hand panels of Figure 5 display density profiles with local time for four altitude ranges. All three density profiles in each panel show similar trends with local time. The observed densities are much higher in the sunlit local times than in the shadowed local times at all four altitude ranges. It may be noted that the plasma density is slightly higher near the terminators than near the subsolar point within the lowest altitude bin, as shown in Figure 5(e). However, these density variations at the sunlit local times are almost within error bars, indicating that they are not highly statistically significant.

5. Discussion and Conclusions

Several observations by RO experiments have suggested that the lunar ionosphere can have electron densities of hundreds of cm^{-3} , which has aroused an intense curiosity in the planetary science community. A few mechanisms have been proposed to interpret the formation of such a dense lunar ionosphere. The mechanism proposed by Savich (1976) relied on trapping of photoionized exospheric neutrals inside lunar crustal magnetic fields, thus preventing them from being rapidly swept away as pickup ions and forming a dense ionosphere with a plasma density of $\sim 1000 \text{ cm}^{-3}$. However, the locations of high plasma densities observed by RO experiments are mostly not near regions with relatively strong remanent magnetic fields (Ando et al. 2012). Another mechanism suggested by Bauer (1996) explained RO observations by a photoelectron layer created by the photoemission of electrons from the lunar surface, but the sheath scale height (on the order of meters) is much shorter than that required to explain a dense lunar ionosphere of RO observations (e.g., Gard & Tunaley 1971; Poppe & Horányi 2010). The third mechanism proposed was “dust-electrons” created by the photoemission of electrons from lunar exospheric dust, as suggested by Stubbs et al. (2011). However, dust measurements from the Lyman Alpha Mapping Project instrument aboard the Lunar Reconnaissance Orbiter (LRO) have revealed that the observed dust density is not sufficient to produce the electron density as estimated by the RO measurements (Feldman et al. 2014). Several other proposed mechanisms require high neutral concentrations to produce the observed electron concentrations, but their assumed neutral concentrations are typically higher than measurements or upper limits determined by other experiments (Sridharan et al. 2010; Cook et al. 2013).

Daily et al. (1977) argued that electron densities inferred by RO experiments are extremely high compared to theoretical estimates and might be an artifact of the observations. The

traditional RO experiments used a single-spacecraft method. A major drawback of this method is that the density fluctuations in the terrestrial ionosphere and interplanetary space along the ray path can lead to errors in the derived electron content near the lunar surface. Based on the LRO single-spacecraft RO observations, Withers et al. (2021) reported that the near-surface electron density in the dayside lunar ionosphere can sporadically exceed $\sim 300 \text{ cm}^{-3}$, but such detections occur infrequently. They suggested that these large electron densities are probably spatially localized, episodic, or both. In addition, the projected uncertainty in these measurements near the surface is $\sim 500 \text{ cm}^{-3}$, which is greater than the derived electron density. To cope with the large error caused by the terrestrial ionosphere and interplanetary space plasma, a dual-spacecraft method was therefore developed. This new method uses two subsatellites at the same time, to remove the contributions from the terrestrial ionosphere and interplanetary plasma. However, using this dual-spacecraft RO method, Ando et al. (2012) did not observe a stable electron density enhancement near the surface as reported by traditional single-spacecraft RO experiments, even on the sunlit side.

Recently, Ambili & Choudhary (2022) proposed a numerical photochemical model in order to explain large plasma densities near the lunar surface observed from RO experiments. This model predicts that the electron density at altitudes below 40 km near the equator is at least $\sim 200 \text{ cm}^{-3}$ in any local-time sector for the case when the lunar environment interacts with the solar wind. They attributed the production of high electron densities to ionization processes of CO_2 , and suggested CO_2^+ as the major ion species. Surprisingly, the density was shown to be much higher at midnight than at noon in their model. At midnight, the photoionization production rate is near zero, and thus charge exchange reactions with solar wind ions and electrons are considered as the major source for ionization in their model. However, the very low density of solar wind plasma in the lunar wake should highly suppress these charge exchange reactions, casting doubt on charge exchange as a major source of ionization at midnight. Meanwhile, works by Halekas et al. (2018) and Poppe et al. (2022) have revealed no non-solar-wind ion densities higher than 0.3 and 0.1 cm^{-3} , respectively, within the sunlit portion of the lunar environment, in disagreement with high ion densities predicted by the model of Ambili & Choudhary (2022).

The electron density in the lunar ionosphere has been under debate for several decades. In this paper, for the first time, we provide event analyses and statistical density profiles with altitude and local time from in situ measurements. These can serve as a reference for a comparison between in situ measurements and RO observations. The ARTEMIS ESA instrument can measure charged particles over a broad energy range. In addition to solar wind particles, these measured particles include cold ions and electrons produced from the ionization of neutrals in the lunar exosphere and/or direct production from the surface. In contrast to plasma densities of hundreds of cm^{-3} suggested by RO experiments, ARTEMIS measurements reveal no densities at altitudes between 10 and 50 km during the ten-year period of 2012–2021 that exceed 35 cm^{-3} . The average density observed in this near-surface altitude range is about 5.4 cm^{-3} . It should be noted that these measurements do not cover regions with altitudes lower than 10 km or with high latitudes, due to limitations of the ARTEMIS orbits. Thus, we cannot make any definitive

statements regarding the plasma density in these regions. Our density profiles show that the plasma density at altitudes below 400 km is much greater in the sunlit sector than in the shadowed sector, with $1\text{--}10\text{ cm}^{-3}$ for the former and $<0.1\text{ cm}^{-3}$ for the latter, as expected if the dominant source of plasma is the solar wind, which is largely excluded from the lunar wake region near the shadowed surface. This result is well supported by electron densities derived from the upper hybrid resonance frequencies in the electric field time–frequency spectra observed by the waveform capture instrument on board the SELENE/KAGUYA (Selenological and Engineering Explorer) lunar orbiter. As reported by Goto et al. (2011), these derived densities statistically exhibit a clear day–night asymmetry, with densities of $1\text{--}5\text{ cm}^{-3}$ on the dayside and densities of $<0.1\text{ cm}^{-3}$ on the nightside, providing no evidence for a high electron density layer near the lunar surface. In addition, Goto et al. (2011) proposed a new method for examining the lunar ionosphere by using the interference pattern caused by auroral kilometric radiation (AKR) on the electric field time–frequency spectra observed by the natural plasma wave receiver on board the SELENE. The example event analyzed in their paper using this new method was observed during a period when the SELENE was orbiting in a midnight region. By examining the phase difference between the direct AKR from the Earth and the AKR reflected by the lunar surface or a possible lunar ionosphere, no dense ionosphere was found in this region, consistent with our nightside density profiles and event analysis. In conclusion, ARTEMIS observations suggest that the plasma density near the lunar surface (altitudes below 400 km) is predominantly modulated by solar wind plasma, with no significant contribution by a global dense lunar ionosphere.

Acknowledgments

The authors acknowledge NASA contract NAS5-02099 and V. Angelopoulos for the use of data from the THEMIS-ARTEMIS Mission. We thank C. W. Carlson and J. P. McFadden for the use of ESA data, and thank J. W. Bonnell and F. S. Mozer for the use of EFI data. We appreciate K. H. Glassmeier, U. Auster, and W. Baumjohann for the use of FGM data provided under the lead of the Technical University of Braunschweig and with financial support through the German Ministry for Economy and Technology and the German Center for Aviation and Space (DLR) under contract 50 OC 0302. This work was supported by the Solar System Exploration Research Virtual Institute through cooperative agreements 80NSSC20M0022 and 80NSSC20M0060, as well as the Lunar Data Analysis Program through grant 80NSSC20K0311. The two-probe ARTEMIS measurements are all publicly available through <http://themis.ssl.berkeley.edu/data/themis/thb/12/> and <http://themis.ssl.berkeley.edu/data/themis/thc/12/>.

Facilities: THEMIS-ARTEMIS (ESA, EFI, and FGM).

ORCID iDs

Han-Wen Shen  <https://orcid.org/0000-0001-6733-5065>
 Jasper S. Halekas  <https://orcid.org/0000-0001-5258-6128>
 Andrew R. Poppe  <https://orcid.org/0000-0001-8137-8176>

References

- Ambili, K. M., & Choudhary, R. 2022, *MNRAS*, **510**, 3291
 Ando, H., Imamura, T., Nabatov, A., et al. 2012, *JGRA*, **117**, A08313
 Angelopoulos, V. 2008, *SSRv*, **141**, 5
 Angelopoulos, V. 2011, *SSRv*, **165**, 3
 Auster, H., Glassmeier, K., Magnes, W., et al. 2008, *SSRv*, **141**, 235
 Bauer, S. 1996, *Anzeiger Abt. II*, **133**, 17, https://www.researchgate.net/publication/242512939_Limits_to_a_Lunar_Ionosphere
 Bonnell, J., Mozer, F., Delory, G., et al. 2008, *SSRv*, **303**
 Bosqued, J., Lormant, N., Rème, H., et al. 1996, *GeoRL*, **23**, 1259
 Choudhary, R., Ambili, K., Choudhury, S., Dhanya, M., & Bhardwaj, A. 2016, *GeoRL*, **43**, 10
 Chu, F., Halekas, J. S., Cao, X., et al. 2021, *JGRA*, **126**, e2020JA028880
 Colburn, D. S., Currie, R., Mihalov, J., & Sonett, C. 1967, *Sci*, **158**, 1040
 Cook, J. C., Stern, S. A., Feldman, P. D., et al. 2013, *Icar*, **225**, 681
 Daily, W. D., Barker, W. A., Clark, M., Dyal, P., & Parkin, C. W. 1977, *JGR*, **82**, 5441
 Elphic, R. C., Funsten, H. O., III, Barraclough, B. L., et al. 1991, *GeoRL*, **18**, 2165
 Elsmore, B. 1957, *PMag*, **2**, 1040
 Feldman, P. D., Glenar, D. A., Stubbs, T. J., et al. 2014, *Icar*, **233**, 106
 Goto, Y., Fujimoto, T., Kasahara, Y., Kumamoto, A., & Ono, T. 2011, *EP&S*, **63**, 47
 Grad, R. J. L., & Tunaley, J. K. E. 1971, *JGR*, **76**, 2498
 Halekas, J., Angelopoulos, V., Sibeck, D., et al. 2011, *SSRv*, **165**, 93
 Halekas, J., Bale, S., Mitchell, D., & Lin, R. 2005, *JGRA*, **110**, A07222
 Halekas, J., Brain, D., Lin, R., & Mitchell, D. 2008, *AdSpR*, **11**, 1319
 Halekas, J., Poppe, A., Harada, Y., et al. 2018, *GeoRL*, **45**, 9450
 Halekas, J., Poppe, A., McFadden, J., et al. 2014, *GeoRL*, **41**, 7436
 Hodges, R., Hoffman, J., & Johnson, F. S. 1974, *Icar*, **21**, 415
 Huebner, W., & Mukherjee, J. 2015, *P&SS*, **106**, 11
 Imamura, T., Nabatov, A., Mochizuki, N., et al. 2012, *JGRA*, **117**, A06303
 Johnson, F. S. 1971, *RvGeo*, **9**, 813
 Lin, R., Mitchell, D., Curtis, D., et al. 1998, *Sci*, **281**, 1480
 Lue, C., Futaana, Y., Barabash, S., et al. 2011, *GeoRL*, **38**, L03202
 McFadden, J., Carlson, C., Larson, D., et al. 2008a, *SSRv*, **141**, 477
 McFadden, J., Carlson, C., Larson, D., et al. 2008b, *SSRv*, **141**, 277
 Mozer, F. 1973, *SSRv*, **14**, 272
 Murkett, A. 1979, *PhyEd*, **14**, 87
 Nishimura, Y., Bortnik, J., Li, W., et al. 2013, *JGRA*, **118**, 664
 Ogilvie, K., & Ness, N. F. 1969, *JGR*, **74**, 4123
 Ogilvie, K., Steinberg, J., Fitzenreiter, R., et al. 1996, *GeoRL*, **23**, 1255
 Pedersen, A., Mozer, F., & Gustafsson, G. 1998, in *Measurement Techniques in Space Plasmas: Fields*, ed. R. F. Pfaff, J. E. Borovsky, & D. T. Young (Washington, DC: American Geophysical Union), 1
 Pluchino, S., Schilliro, F., Salerno, E., et al. 2008, *MSAIS*, **12**, 53
 Poppe, A., & Horányi, M. 2010, *JGRA*, **115**, A08106
 Poppe, A. R., Halekas, J. S., & Harada, Y. 2022, *JGRE*, **127**, e2022JE007422
 Reasoner, D. L., & Burke, W. J. 1972, *JGR*, **77**, 6671
 Russell, C., & Lichtenstein, B. 1975, *JGR*, **80**, 4700
 Saito, Y., Nishino, M. N., Fujimoto, M., et al. 2012, *EP&S*, **64**, 83
 Saito, Y., Yokota, S., Asamura, K., et al. 2010, *SSRv*, **154**, 265
 Sarantos, M., Killen, R. M., Glenar, D. A., Benna, M., & Stubbs, T. J. 2012, *JGRA*, **117**, A03103
 Savich, N. 1976, in *Space Research XVI: Proc. of the Open Meetings of Working Groups on Physical Sciences* (Berlin: Akademie-Verlag), 941
 Sawyer, R., & Halekas, J. 2022, *JGRA*, **127**, e2022JA030740
 Siscoe, G., Lyon, E., Binsack, J., & Bridge, H. 1969, *JGR*, **74**, 59
 Sonett, C., & Mihalov, J. 1972, *JGR*, **77**, 588
 Sridharan, R., Ahmed, S., Pratim Das, T., et al. 2010, *P&SS*, **58**, 1567
 Stern, S. A. 1999, *RvGeo*, **37**, 453
 Stubbs, T. J., Glenar, D., Farrell, W., et al. 2011, *P&SS*, **59**, 1659
 Tripathi, K. R., Choudhary, R., Ambili, K., et al. 2022, *MNRAS: Lett.*, **515**, L61
 Tsunakawa, H., Takahashi, F., Shimizu, H., Shibuya, H., & Matsushima, M. 2015, *JGRE*, **120**, 1160
 Vyshlov, A. S. 1976, in *Space Research XVI: Proc. of the Open Meetings of Working Groups on Physical Sciences* (Berlin: Akademie-Verlag), 945
 Vyshlov, A. S., & Savich, N. A. 1979, *CosRe*, **16**, 551
 Withers, P., Stubbs, T., & Mazarico, E. 2021, *AdSpR*, **67**, 4099